UAS Photogrammetry for Precise Digital Elevation Models of Complex Topography: A Strategy Guide

Melanie Elias[1], Steffen Isfort[1], Anette Eltner[1], Hans-Gerd Maas[1]

[1] Institute of Photogrammetry and Remote Sensing, TUD Dresden University of Technology, Germany - (melanie.elias, steffen.isfort, anette.eltner, hans-gerd.maas)@tu-dresden.de

Keywords: UAS, Image Orientation, Georeferencing, Terrain Modeling, Structure-from-Motion.

Abstract

The presented research investigates different strategies to acquire high-precision digital elevation models (DEMs) of complex and inaccessible terrain using Structure-from-Motion and Multi-View Stereo applied to data of an unoccupied aerial system (UAS) equipped with real-time-kinematic (RTK)-GNSS. The survey scenarios are taken from real-life situations and thus, in comparison to many previous studies, provide information on how to operate under challenging conditions in difficult terrain. Among others, the study examines the influence of different flight configurations (parallel axes and cross-grid), flight altitudes (relative to ellipsoid or terrain) and associated variations in ground sampling distance, image orientations (nadir and oblique), advanced camera self-calibration techniques and georeferencing strategies in image block processing (direct and integrated) on the overall accuracy of the resulting DEMs. Random and systematic errors, including spatial patterns such as doming and bowling, are quantified using check points and differences between DEM calculations and independently acquired surface data from laser scans. This comprehensive analysis contributes valuable insights for UAS-based analysis of complex terrain with improved accuracy in DEM generation and subsequent applications like change detection.

1. Introduction

UASs equipped with cameras are important and well-established instruments for the flexible spatiotemporal high-resolution monitoring of environmental processes in many geoscientific applications, e.g. in glaciology (Belloni et al., 2022), at relatively low costs. Multi-image processing techniques such as structure-from-motion (SfM) and multi-view-stereo (MVS), implemented in numerous user-friendly software packages, enable the calculation of DEMs. By comparing multi-temporal DEMs, changes can be determined as a function of the ground sampling distance (GSD) in the four-dimensional domain.

The commercialization of low-cost surveying UASs with fixed cameras and RTK-GNSS, such as the DJI Phantom 4 RTK, elevated UAS photogrammetry in geosciences. However, camera construction and native image pre-processing routines lead to lens distortion characteristics that cannot be adequately described by standard camera calibration models integrated in many SfM software packages (Liebold et al., 2023; Hastedt et al., 2021). This results in spatial errors in DEM calculation called doming/bowling and can be reduced by, e.g., well-distributed ground control points (GCPs), the use of cross-grid flights with varying altitudes, camera pre-calibration or the use of additional oblique images (e.g. Stark et al., 2021; James et al., 2020; Sanz-Ablanedo et al., 2020; Nesbit and Hugenholtz, 2019; Gerke and Przybilla, 2016; Eltner and Schneider, 2015; James and Robson, 2014). Using UASs with dual-frequency GNSS receivers can increase accuracy and allows for direct georeferencing of the image block in real-time or post-flight by RTK-GNSS or post-processed kinematic (PPK). These image position information, determined to within a few centimeters, significantly improve the estimation of the interior orientation parameters (IOP) and stabilize the image block in the bundle block adjustment (e.g. Kersten and Lindstedt, 2022; Przybilla et al., 2020). However, an important aspect highlighted in many of these studies is the presence of a precisely measured and consistent GCP network.

The measurement of GCPs is time-consuming, contrary to the idea of flexible UAS surveying or simply not possible in steep and inaccessible terrain. This raises the question of whether GCPs can be greatly reduced or avoided by using advanced image acquisition and analysis strategies without compromising accuracy. Schulze et al. (2022); Liu et al. (2022) and Przybilla et al. (2020) examined DEMs from SfM using PPK-georeferenced images. They found that one GCP is necessary to correct systematic errors such as height offsets and doming. However, the investigations were mainly focused on terrain with moderate relief, where systematic errors are expected to be higher due to correlations of principal distance and depth direction. Belloni et al. (2022) evaluated the use of PPK georeferencing in UAS photogrammetry for 3D surveying of glaciers in the Alps and showed accuracies of a few centimeters in the resulting DEMs, even when working without GCPs. However, PPK requires an own separate base station and advanced processing strategies, while the use of RTK-GNSS requires only a stable mobile connection to a correction positioning service providing data from virtual base stations, e.g. Kersten and Lindstedt (2022).

This study provides an applied meta-analysis of the approaches mentioned in the literature focusing on DEM generation in inaccessible, glacial terrain. Attention is given to the inner precision of 3D point cloud reconstruction as well as random and systematic errors. The overall goal is to guide experts in the efficient calculation of DEMs by UAS photogrammetry for environmental monitoring, especially in complex terrain, with information on the respective accuracies to be achieved in DEM calculation and to identify possible sources of error. The analyzes include image data captured by the UAS DJI Phantom 4 RTK with RTK-GNSS in two epochs at the glacier Bøverbreen under different observation conditions.

This contribution has been peer-reviewed. The double-blind peer-review was conducted on the basis of the full paper.
https://doi.org/10.5194/isprs-annals-X-2-2024-57-2024

We include the following scenarios in the analysis:

1. influence of **flight patterns & combinations**: parallel-axes (PA) and cross-grid (CG) flights with nadir and 45°oblique (O) images.
2. influence of **flight altitude** regarding GSD variability, image overlap and image block stability: relative to WGS84 ellipsoid and relative to topography.
3. influence of **georeferencing strategy**: direct and integrated georeferencing. In this study, both imply integrated sensor orientation, e.g. as in Eltner and Sofia (2020), without (direct georeferencing) and with (integrated georeferencing) the use of GCPs.

2. Materials and Methods

2.1 Study Area

The study area (449800E, 6825150N in WGS84/UTM32N) comprises the western, partly debris-covered outlet glacier of the Smørstabbreen glacier, called Bøverbreen, in the Norwegian Jotunheimen National Park (Figure 1).

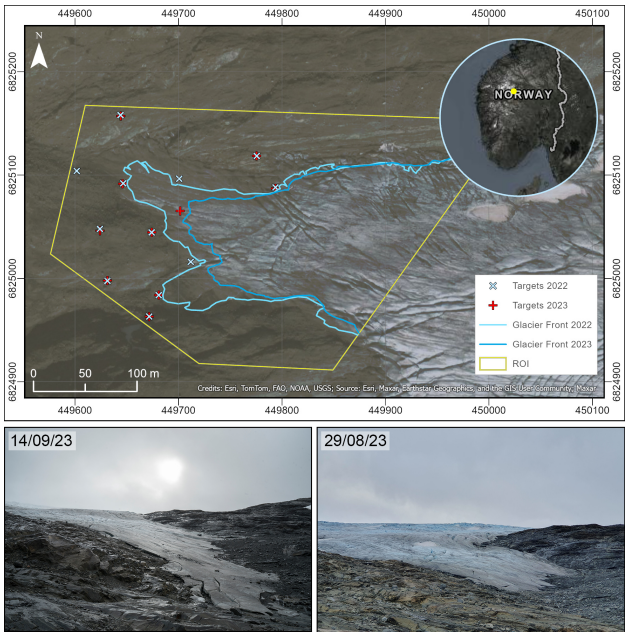

Figure 1. Study area Bøverbreen, Norway (Proj.: UTM32N).

The glaciers in Jotunheimen are experiencing a strong retreat. Andreassen et al. (2020) examined the changes between 1960 and 2010 and showed a reduction in geodetic mass balance of -0.21 m w.e.a^{-1}. The extent of the glaciers decreased by 15% in 50 years, which corresponds to a volume of about 850 km^3. Observing changes in ice mass distribution requires knowledge on the glacier margins, which are often automatically derived from optical remote sensing data and stored in glacier inventories, e.g. Pfeffer et al. (2014). However, the marginal areas of the debris-covered glacier tongues, such as Bøverbreen in parts, are quite difficult to distinguish from ambient terrain in such data and are often misinterpreted even when digitized manually. Regularly generated DEMs and DEM of difference (DoD) analyzes improve the measurement in these critical areas by detecting changes in the margin geometrically. The Bøverbreen is characterized by loose debris and exposed, polished rocks. Accessibility is limited to a small area at the front of the glacier terminus, especially after days with high precipitation, when the glacier-cut rocks are difficult to access. Due to the valley floor, high wind speeds and rapidly changing weather conditions are to be expected. Thus, Bøverbreen is an excellent place to investigate the influence of different UAS flight and georeferencing strategies on the DEM accuracy.

2.2 UAS and Flight Pattern

The applied UAS DJI Phantom 4 RTK integrates the camera FC6310R with fixed wide-angle lens and 1” complementary metal-oxide-semiconductor (CMOS) sensor (specs in Table 1).

General specs	
Take-off Weight	1391 g
Critical Wind Speeds	$<$10 m/s / 36 km/h
Flight Time	ca. 30 min
Max. Broadcast Range	7 km
Working Temperatures	0°C-40°C (Aircraft, Remote Control) -10°C-40°C (Battery)
Camera	
Type	FC6310R
Focal Length	8.8 mm /24 mm (35-mm equivalent)
Sensor Size	Sony 1”CMOS (global shutter)
Sensor Resolution	5472 x 3648 pixels
Pixel Pitch	2.41 µm
GNSS	
Frequencies	GPS: L1/L2 GLONASS: L1/L2 BeiDou: B1/B2 Galileo: E1/E5a
Positioning Accuracy (RTK-GNSS)	Vertical: 1.5 cm + 1 ppm (RMS) Horizontal 1.0 cm + 1 ppm (RMS)

Table 1. Manufacturer specs on the UAS DJI Phantom 4 RTK.

2.2.1 DJI GS RTK Mission Planning. Image flight planning was done with the DJI GS RTK flight control and planning software. Four photogrammetric flight modes are offered:

- 2D Photogrammetry: PA, altitude above WGS84 ellipsoid
- 3D Photogrammetry: CG (two crossed PA), altitude above WGS84 ellipsoid
- 3D Photogrammetry: PA + four oblique images, altitude above WGS84 ellipsoid
- Terrain Awareness Mode: PA, altitude above DEM

In all modes, the flight strips are planned automatically based on a region of interest (ROI), e.g. given by a KML file, as well as image block parameters such as flight altitude (with automatic calculation on the resulting GSD) and image overlap (along-track/ across-track) including calculations on flight speed and distances between the image centers. Image parameters such as exposure time and f-stop are adjusted automatically during the flight depending on the prevailing light situation. The images are stored in JPEG format. An important setting is to disable DJI’s built-in and by default enabled generic lens distortion correction, as it can interfere with the estimation of decentering lens distortion parameters in subsequent photogrammetric processing (James et al., 2020).

2.2.2 DJI GS RTK Terrain Awareness Mode. Since Firmware v02.01 (release 05/2019), DJI GS RTK offers the *Terrain Awareness Mode* for Phantom 4 RTK enabling flight missions with altitudes relative to the surface. Flying in terrain following mode requires a gridded DEM of the ROI in WGS84 reference system with ellipsoidal heights. A known issue when using this mode is the circumstance that the UAS immediately flies to the altitude of the first waypoint after takeoff, which is

This contribution has been peer-reviewed. The double-blind peer-review was conducted on the basis of the full paper.
https://doi.org/10.5194/isprs-annals-X-2-2024-57-2024 | © Author(s) 2024. CC BY 4.0 License.

the sum of the terrain height below the first targeted waypoint in the DEM plus the defined flight altitude. If the take-off point is at an altitude of, e.g., 1500 m and the first waypoint is lower, e.g., at 1400 m (1300 m terrain altitude plus 100 m flight altitude), the UAS will not take off. The scenario is even worse if the altitude of the first waypoint is slightly above the take-off point. In the given example, if the altitude of the first waypoint is 1510 m, the UAS flies directly to the first waypoint at an altitude of only 10 m, which poses a risk of collision, e.g. Girod (2021). Given good visibility, a solution is flying manually to the first waypoint before starting the planned image flight. Alternatively, the take-off point should be high in the terrain close to the ROI margin as the first waypoint is usually at the ROI margin and close to the take-off point, thus it can be reached safely in this way. However, these conditions may not always be met in geoscientific investigations.

2.2.3 Direct image georeferencing. An integrated dual-frequency RTK-GNSS receiver was used to obtain position information with an accuracy of a few centimeters utilizing the Norwegian positioning service CPOS. The GNSS-antenna lever arm was calibrated by the manufacturer DJI and is directly applied to the image data. Furthermore, rotation information was captured by the UAS' built-in inertial measurement unit (IMU).

2.3 Study Design

Four image block configurations were included in the investigation comprising PA and CG nadir-image flights with and without added oblique images. Performing PA flights, the UAS was heading north-south. For CG flights, the north-south PA pattern was added with an east-west PA flight. Like in Schulze et al. (2022) and Nesbit and Hugenholtz (2019), single 45° oblique images were additionally added to the PA and CG image blocks resulting in a total of four image block configurations from the selected flight patterns: PA, CG, PAO and CGO. The flight strips are illustrated in Figure 2.

The study was conducted in 2022 and 2023 with the same ROI and flight pattern but variation in the strategy of flight altitude determination, i.e. relative to WGS84 reference ellipsoid (2022) and relative to terrain (2023) that is explained more in detail below. Details on the missions are given in Table 2.

Different georeferencing strategies were tested to figure out the accuracy potential in terms of random and systematic errors performing direct georeferencing without any GCP or integrated georeferencing with a few GCPs. In regard of applying direct georeferencing, pitfalls to be expected are reduced accuracies due to terrain shading impacting line of sights to satellites and potential disconnections to the positioning service.

2.3.1 Mission 2022. The first UAS flights were carried out on 14th September 2022. As part of the study design, 12 uncoded circular targets (black/white, Ø 20 cm), serving as GCPs and check points (CPs), were temporarily and uniformly placed in the accessible front area of the glacier tongue and measured with the Emlid Reach RS2 RTK-GNSS receiver using CPOS (observation time per target ca. 15 seconds). The configuration is shown in Figure 1. The mean Root Mean Square Error (mRMSE) of the target coordinates amounts to 1.1 cm in XY- and 1.5 cm in Z-direction.

The weather conditions and corresponding limited visibility prevented the use of the Terrain Awareness Mode due to issues with the take-off point. The flight planning for PA and CG was carried out in 2D photogrammetry mode. To achieve a sufficiently high image overlap and stable image block flying with a fixed altitude above steep terrain, the overlap was set to 90/80 (90% along-track, 80% across-track) with an altitude of 115 m for the first PA flight. The second PA flight to complete the CG pattern was flown at a lower altitude of 100 m with a set image overlap of 80/70 and to stabilize the image block, according to, e.g., Kersten and Lindstedt (2022). Single oblique images were taken at the ends of the two flights. The GSD ranges between 0.5 cm and 3.6 cm at nadir. Each image is accompanied by position information from RTK-GNSS with accuracies of a few centimeters (standard deviations (STDs) given in DJI metadata).

In terms of accuracy assessment and detection of any systematic deformation in the processed image blocks, terrestrial laser scanning (TLS) data was captured at the same date as the UAS flights with a RIEGL VZ-400i using 21 scan positions distributed in the accessible front area of the glacier. Georeferencing was done using temporary cylindrical targets, measured with RTK-GNSS.

2.3.2 Mission 2023. The second UAS flights were conducted on 29th August 2023. Again, 10 uncoded targets were placed and measured in an almost identical configuration as in 2022 with minor variations due to the strongly changed glacier front (see Figure 1). The number varies due to the target availability.

The weather and wind conditions allowed for climbing up to a high terrain point for take-off enabling the use of DJI's Terrain Awareness Mode and thus image-block configurations with nearly constant GSD. Flight planning was conducted similar to the schemes in 2022, having PA and CG flights planned but this time both patterns exhibit 80/70 overlap at a terrain-adjusted flight altitude of 50 m. For this purpose, the freely available DEM *NDH Jostedalsbreen 2pkt 2020* was used. The DEM was acquired in year 2020 by airborne laser scanning and was provided by the Norwegian mapping authority *Kartverket* in a grid (cell size 0.5 m) in the ETRS89/UTM32N reference system with orthometric heights in the NN2000 vertical reference frame. The authorities' accuracy requirements claim height accuracies of $<$10 cm (Terratec, 2020). For transformation to ellipsoidal heights and to geographic coordinates, as required by DJI GS RTK, an in-house developed tool was used. The accuracies (STDs) of the RTK-GNSS positions revealed during this campaign increased uncertainties in the determination of the altitude component, which cannot be explained even after analyzing the lines of sight to available satellites (no anomalies, number of satellites at least 25).

Additional TLS data was acquired from 12 scan positions in the glacier's reduced front area and georeferenced by RTK-GNSS-measured cylindrical targets similar to the mission in 2022.

2.4 Data Processing and Analyzes

An automatic SfM-MVS workflow using Agisoft Metashape Python API (version 2.0.2) was implemented to perform bulk processing for all image block and georeferencing configurations to be analyzed. The image measurement of the targets was done in advance by interactive point selection in all images of a survey. The general workflow is shown in Figure 3. In total 16 image block configurations (called ”chunks”) were processed; four image blocks (PA, PAO, CG, CGO) with four georeferencing strategies: direct georeferencing using no GCPs, integrated

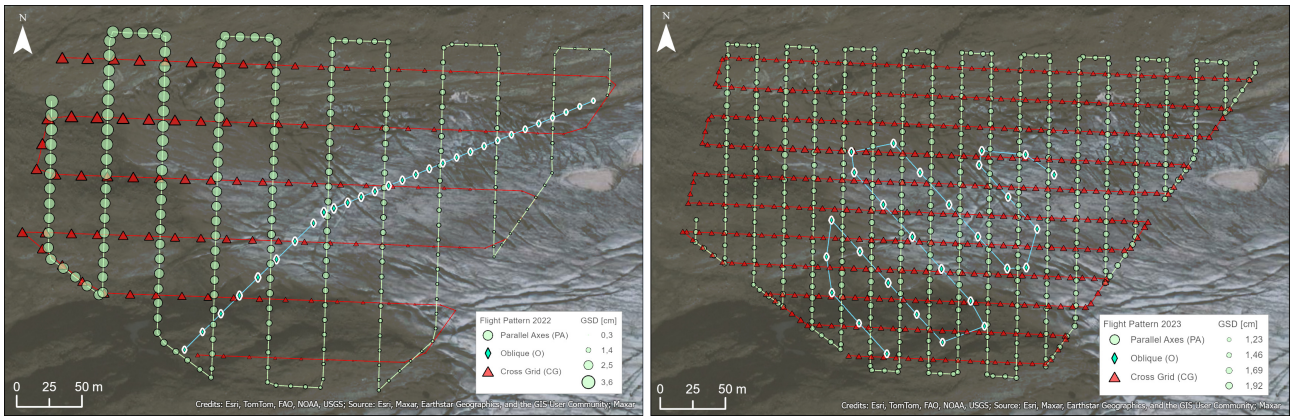

Figure 2. Flight pattern in 2022 (left) and 2023 (right). Variations in the GSDs due to different flight altitude configurations.

		2022				2023		
		PA	**O1**	**CG**	**O2**	**PA**	**CG**	**O**
Image Block	Rel. UAS Altitude	115 m (±3 cm) above WGS84 ellipsoid		100 m (±3 cm) above WGS84 ellipsoid		50 m (±5 cm) above DTM Imitation fineness: 10 m (default)**		
	Overlap (%)	90/80	90/80	80/70	80/70	80/70	80/70	80/70
	Nadir-GSD (cm)	2.0 (0.4-3.6)	-	1.6 (0.3-3.1)	-	1.6 (1.3-1.9)	1.7 (1.2-1.9)	-
	Time (s)*	2.9 ± 0.5	3.0 ± 0.9	6.6 ± 0.5	6.7 ± 0.5	2.5 ± 0.5	2.6 ± 0.5	8.9 ± 0.3
	Distance (m)*	11.2 ± 0.7	11.0 ± 1.1	19.5 ± 1.5	19.8 ± 0.2	9.3 ± 1.3	9.4 ± 1.3	30.9 ± 6.6
	Image Count	238	21	118	8	438	418	25
Image Params	Exposure Time (s)*	1/500-1/100	1/320-1/160	1/500-1/100	1/320-1/160	1/640-1/320	1/800-1/320	1/640-1/240
	F-Stop*	F4.0-F5.6	F4.5-F5.6	F4.0-F5.6	F4.5-F5.6	F5.0-F6.3	F5.0-F7.1	F5.0-F6.3
	ISO	100					100	
	DJI Lens correction	disabled					disabled	
RTK (STD)	Lat (m)	0.01	0.01	0.02	0.01	0.02	0.02	0.01
	Lon (m)	0.02	0.02	0.02	0.02	0.02	0.02	0.02
	Altitude (m)	0.04	0.04	0.04	0.03	0.12	0.09	0.09
Flight Mission	Flight Time (min)	11:25	01:03	12:52	00:46	18:12	17:56	04:00
	Flight Speed (m/s)*	3.9 ± 0.8	3.8 ± 0.8	3.0 ± 0.3	3.0 ± 0.2	3.9 ± 1.0	3.8 ± 1.0	3.5 ± 0.8
	Air Speed / Gusts (m/s)	4.8 / 6.7		4.8 / 6.7		1.6 / 4.2	1.6 / 4.2	1.0 / 3.7
	Weather conditions	closed cloud cover, light fog, freezing rainfall					cloudy, dry	
	Temperature (°C)	2.4		2.3		6.7	6.7	7.4

Table 2. Mission details (epochs 2022 & 2023). *Automatically set parameters. **DJI imitation fineness: Flight path stabilization by smoothing the DEM (default kernel size: 10 m) to prevent the UAS from climbing and descending on terrain irregularities.

georeferencing using one GCP at the take-off point with a focus on the practical implementation in difficult to access terrain, and integrated georeferencing using four and nine GCPs evenly distributed in the image block. Any targets not used as GCPs served as CPs. As far as possible, the same target positions were used in both epochs (see Figure 1).

The images’ pose information from RTK-GNSS and IMU as well as the manufacturer’s camera pre-calibration parameters served as an initial estimate running self-calibration and bundle block adjustment in SfM. In this regard, camera self-calibration was conducted using the standard modeling of the IOP and lens distortion parameters according to Brown (1971). Furthermore, Fourier series modeling, implemented in Metashape based on Tang et al. (2012) since version 1.6.0, was used as, according to Hastedt et al. (2021), it allows the modeling of aspherical lens distortions as they occur in the camera used in this study.

As a result, 16 image blocks were processed including the estimation of the IOP and exterior orientation parameters (EOP) and the 3D point cloud coordinates. Furthermore, statistics, e.g. residuals at the GCPs and CPs, for the accuracy assessment were included. MVS was applied for dense point cloud reconstruction based on the processed image blocks. In this regard, the images were downscaled by a factor of two (quartered image resolution) and subsampled to a point distance of 2 cm for performance reasons. The dense point clouds are used for DoD analyzes with the independently captured TLS data to recognize any spatial error patterns in the dense clouds.

Alignment of the single TLS scans was done in RiSCAN Pro 2.8 with maximum residuals of less than 2 cm between the scans in both epochs. No systematic deviations are noticeable. Beside some manual outlier filtering, the point clouds were subsampled to a point distance of 2 cm by voxel filtering. Due to reflectivity reasons of the ice and the scanner’s wavelength in near infrared, the TLS data shows gaps on the blank glacier ice. Details on the TLS data are given in (Isfort et al., 2024).

Cross-source registration between UAS and TLS point clouds was done using the georeferencing as basis, followed by a fine registration applying iterative closest point (ICP) registration in manually selected stable areas. Spatial distances were calculated by M3C2 algorithm setting the parameters D (normal calculation) and d (projection) to 0.3 m (see Lague et al., 2013).

The IOP are analyzed for remaining systematics and correlations after self-calibration using standard and advanced Fourier series modeling. Furthermore, the residuals of the EOP to the acquired RTK-GNSS data as well as deviations at the GCPs and CPs are analyzed. Finally, DoD analyzes are performed. Due to the temporal proximity of the TLS- and UAS-derived point clouds, it can be assumed that the glaciated areas are stable during these investigations.

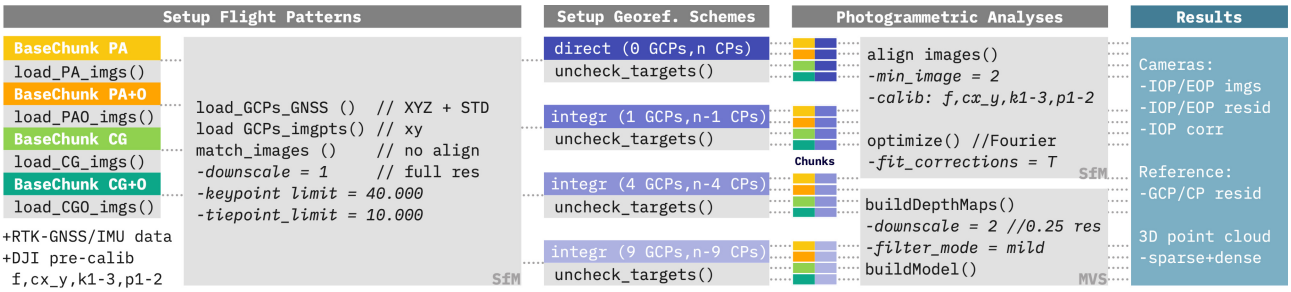

Figure 3. SfM-MVS workflow scheme.

3. Results and Discussion

In the following section, the quality of SfM-based 3D reconstruction is analyzed including the estimated IOP and EOP and the GCP residuals as a measure of precision (only integrated georeferencing). Random and systematic errors are analyzed based on CPs. Any spatial error patterns should be revealed by DoD analyzes.

3.1 Point Cloud Reconstruction

3.1.1 3D point cloud generation was successfully conducted for all tested configurations in both epochs resulting in 2.0–5.5 million tie points in the individual sparse 3D point clouds (see Table 3).

		PA	PAO	CG	CGO
2022	Outlier	98707	108342	134407	143948
	Original	1974133	2166840	2688137	2878957
	TOTAL	1875426	2058498	2553730	2735009
2023	Outlier	175075	180516	284605	289961
	Original	3501481	3610306	5692081	5799210
	TOTAL	3326406	3429790	5407476	5509249

Table 3. Number of reconstructed 3D points from tie point matches before and after 95-percentile filtering.

Reprojection errors were calculated from the reconstructed 3D point coordinates of the tie points projected back into the images. In this context, outliers were eliminated using a 95% percentile filter. In all examined image blocks the median reprojection error was about 0.25 pixels (see Figure 4). The reprojection errors are slightly lower in the 2023 data than in the 2022 data. This is probably due to the almost constant GSD flying at a consistent height above the terrain, higher resolved images providing more features due to lower flight altitudes and more stable image block configurations. The maximum reprojection error increases slightly in both epochs as the number of images increases, which is to be expected. Flight pattern and georeferencing strategy have no significant impact on the reprojection errors and thus the inner precision of the calculated 3D point cloud. This is likely due to the well-determined IOP and lens distortion parameters using pre-calibrated camera parameters and Fourier series modeling in addition to the standard modeling in SfM self-calibration. Also, this might be due to good approximations of the EOP from RTK-GNSS that is the subject of the following analyzes.

3.1.2 IOP. As stated in Hastedt et al. (2021), the use of higher-order Fourier series modeling in SfM self-calibration can significantly reduce systematic errors in image space and improves the estimates of the EOP in object space. Simultaneously, increased correlations between Brown’s lens distortion parameters and the principal distance occur. These statements

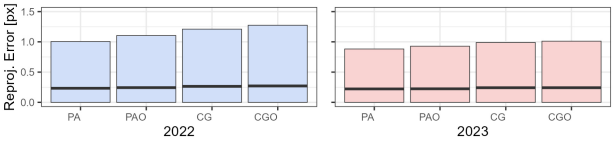

Figure 4. Barplot of min, median (black line) and max reprojection errors (95% percentile) of generated sparse point clouds applying direct georeferencing.

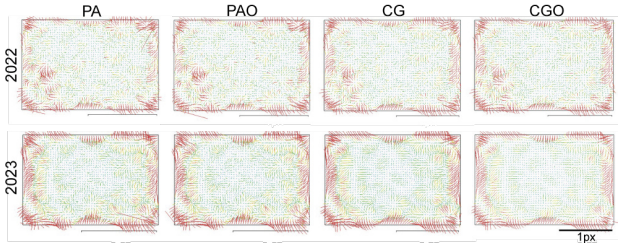

Figure 5. Residual lens distortion plots for the camera FC6310 applying direct georeferencing.

		PA	PAO	CG	CGO
2022	RMS Resid [px]	0.042	0.042	0.042	0.043
	Max Resid [px]	0.477	0.495	0.300	0.455
2023	RMS Resid [px]	0.045	0.044	0.053	0.052
	Max Resid [px]	0.564	0.310	0.273	0.272

Table 4. RMS and maximum of residuals from the distortion plots in Figure 5.

can be confirmed for the estimated FC6130 camera parameters (see Figure 5, Figure 6, and Table 4).

In Figure 5, higher residuals can be seen at the edges of the camera images for all flight patterns regardless of the georeferencing strategy. However, they are far below one pixel and thus, significantly lower than in the works of Stark et al. (2021) and Przybilla et al. (2020) using standard modeling for the camera with remaining residuals of more than one pixel due to the aspheric lens design. The errors at the edges are mainly due to the low image quality of the lens system, which is also reflected in a strong blurring at the image edges. An alternative approach that promises even better results than the applied Fourier series modeling is the recently published bi-radial lens distortion modeling of Liebold et al. (2023), which could be part of further investigations.

The influence of the flight configuration, GSD and selected georeferencing strategy becomes more obvious when focusing on the STDs of the measured IOP and distortion parameters, shown in Figure 7. It was found that the principal distance can be determined most reliably when integrating oblique images into the image block.

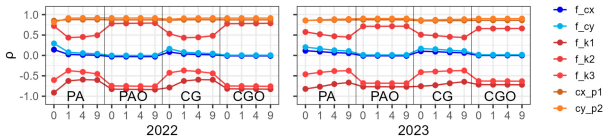

Figure 6. Correlations of the IOP and lens distortion parameters after bundle block adjustment. Numbering of x-axes correspondences to georeferencing strategy (direct: 0 GCPs, integrated: 1, 4 and 9 GCPs).

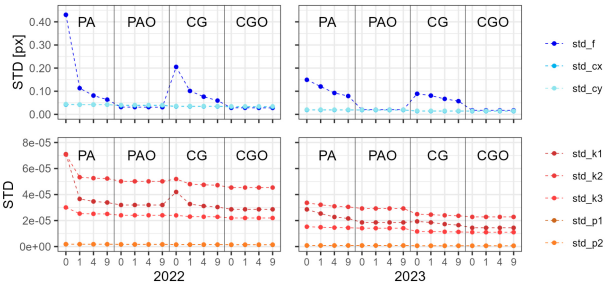

Figure 7. STDs of IOP and lens distortion parameters. Numbering of x-axes according to Figure 6.

3.1.3 GCP residuals. Figure 8 shows the residuals at the GCPs for each configuration and performing integrated georeferencing. The sides of the boxes represent the 25th percentile/ 1st quartile (Q1) and 75th percentile/ 3rd quartile (Q3) known as interquartile range (IQR). The whiskers show the minimum/ maximum value calculated by Q1/Q3 $\mp$ 1.5*IQR, neglecting outliers (black dots).

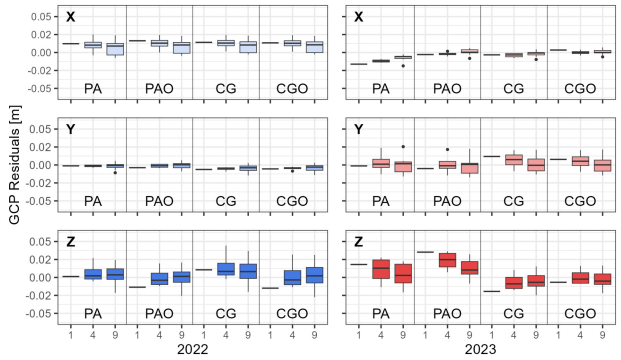

Figure 8. GCP residuals. Limits y-axes: $\pm$ 5 cm. Numbering of x-axes according to Figure 6.

Stark et al. (2021) pointed out that varying image overlap inside an image block could result in errors estimating the EOP and to large deviations at the GCPs. This could not be confirmed for the image blocks in epoch 2022, probably due to good approximations of the EOP, which were not available in the studies by Stark et al. (2021), who used indirect georeferencing based on GCPs.

In the epoch 2023, in which the image blocks have a constant GSD, higher residuals can be seen, particularly in the Z-direction. The reasons for this might lie in the approximated values of the EOP, specifically in the position estimates, measured by RTK-GNSS in 2023, and are examined in more detail below. However, the GCP residuals are still in the range of a few centimeters or less, which is within the tolerance of the measured GCP coordinates, determined with accuracies between 1–2 cm in lateral position (XY) and height (Z).

3.1.4 EOP. Examining the residuals for the calculated image positions with the measured RTK-GNSS data provides information about uncertainties, particularly in the height component. Compared to epoch 2022, relatively large residuals are evident in Z-direction in epoch 2023 (see Figure 9). These result from the RTK-GNSS measurements and not from the selected image flight configuration or georeferencing (see Table 5 and Figure 10). Reasons for the drop in accuracy, which occurred among the first PA flight, cannot be determined: the UAS was in the center of the ROI far from rocks that may cause shadowing. The number of satellites receiving was between 25 and 33 during the entire flight. While the high RTK-GNSS measurement accuracies in epoch 2022 most likely ensured that flight pattern and georeferencing strategy had practically no impact on the magnitudes of the EOP residuals, the great added value of cross-grid flights is evident in the residuals of epoch 2023 (median approx. 0 m, reduced scatter). Processing the 2023 image blocks from parallel axes flight strips (possibly with added oblique images), the EOP residuals improved when using GCPs.

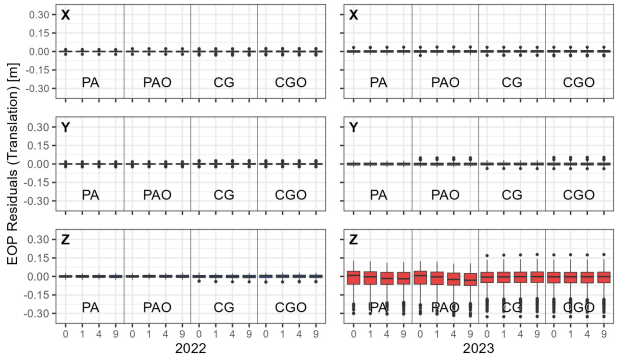

Figure 9. Residuals at the translational EOP in XYZ. Limits y-axes: $\pm$ 30 cm. Numbering of x-axes according to Figure 6.

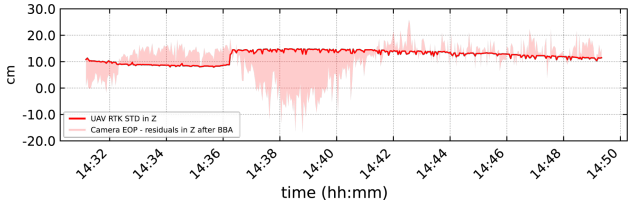

Figure 10. STDs, EOP residuals in z-direction; Parallel axes flight configuration, direct georeferencing.

There are no significant differences in the rotation parameters between the 2022 and 2023 epochs and the respective image block configurations and georeferencing strategies (median residuals $<1°$ for pitch and roll and $\sim 0°$ for heading in all scenarios).

	$\Delta\sigma$ **X [cm]**	$\Delta\sigma$ **Y [cm]**	$\Delta\sigma$ **Z [cm]**
PA Flight	1.6	1.9	12.1
CG Flight	1.6	2.2	8.6
Oblique Flight	1.5	1.7	8.9

Table 5. Mean STD of the RTK-GNSS-based image positions from DJI image tags for all flights in epoch 2023.

3.2 Statistical Analyzes

Random and systematic errors can be detected by statistical analyzes applied to independently captured data. The STDs of the differences between the calculated and measured 3D CPs point to random errors. Comparing SfM-derived DEMs with

3D data from, e.g., TLS allows for the identification of spatial error patterns.

3.2.1 CP residuals. Depending on the georeferencing strategy, 12 (direct, 0 GCPs), 11 (integrated, 1 GCP), 8 (integrated, 4 GCPs), or 3 (integrated, 9 GCPs) targets were left to be used as CPs in epoch 2022. Likewise, 10, 9, 6 and 1 target(s) were used as CPs in epoch 2022. The results of chunks with at least 3 CPs are evaluated below.

Describing the variance in the data by the STD requires normal distributed values while the IQR is more suitable when potential outliers are present. Therefore, the IQR is used instead of the STD as a measure of **random errors**. The IQR in X- and Y-direction are about 1 cm in both epochs and all processed chunks (min/max in 2022: 1.1/1.4 cm; in 2023: 0.7/1.1 cm, see Figure 11). The IQR in Z-direction varies between 1.7 cm and 2.4 cm in 2022 and 1.4 cm and 3.4 cm in 2023. The latter is most likely due to accuracy issues in the RTK-GNSS image position measurement. The IQR and thus the magnitude of random errors is assumed to be smaller for cross-grid flights.

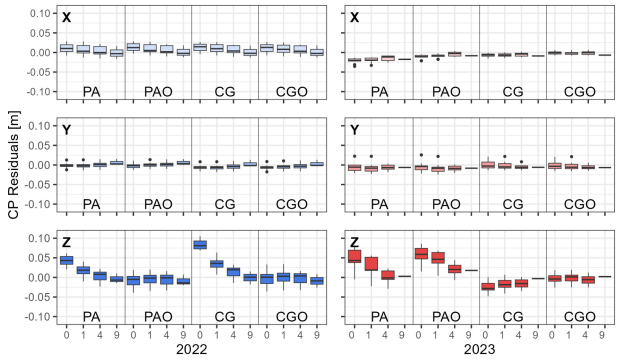

Figure 11. CP residuals. Limits y-axes: ± 10 cm. Numbering of x-axes according to Figure 6.

Systematic errors can be recognized, for example, by the median of the IQR. In 2022, the median of CP deviations in X- and Y-direction was about 0.2 cm, almost independent of the image block configuration but marginally better when a few GCPs were included (max: 0.5 cm [0 GCPs], min: <0.1 cm [4 GCPs]). In 2023, best lateral accuracies were achieved using cross-grid flights with oblique images without noticeable impact of GCPs. The median of CP deviations was <0.5 cm (max: 0.6 cm [CG], min: 0.2 cm [CGO]). In both years, the accuracies in Z-direction are strongly influenced by image block configuration and georeferencing strategy.

In 2022, the processing of nadir flights (PA, CG) shows medial height offsets in range of 4.5–8.0 cm, which is greatly improved if only one GCP is used. Similar findings were made by Schulze et al. (2022). Note, this height offset can apparently also be fully corrected by just adding oblique images without GCPs: median of CP residuals about 0.3 cm; max: 0.5 cm (PAO), min: 0.1 cm (CGO).

In 2023, a slightly different situation is observed. There is also an improvement when using oblique images in addition to nadir images in the block, but best height offset correction is achieved when using cross-grid image configurations. When using images from parallel-axes flights, the height deviations are in the range of 4.0 cm (PA) and 6.0 cm (PAO) without and 2.0 cm (PA) and 5.0 cm (PAO) with the use of one GCP. Without GCPs, only by adding CG images, the height offset is reduced to 0.2 cm (CGO) and 0.4 cm (CG).

3.2.2 DoD analyzes. With a focus on the application in complex terrain, the result of the image block configuration with the smallest deviations from the CPs, i.e. cross-grid flight with few oblique images, is examined for spatial error patterns if no GCPs are used. The DoD results using M3C2 distance calculation between TLS and UAS data are shown in Figure 12 for both epochs. There are mean deviations of less a centimeter in both epochs, which is in the amount of the determined values at the CPs. A significant spatial error pattern in the glacier front area cannot be determined.

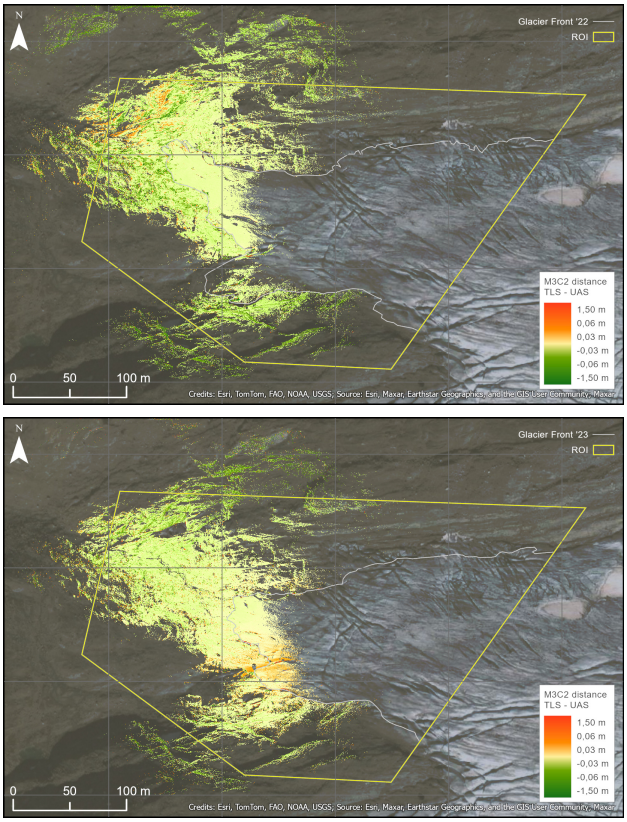

Figure 12. M3C2 distance calculation between 3D point clouds from TLS and UAS flight (cross-grid + oblique, direct georeferencing) in 2022 (top) and 2023 (bottom).

4. Conclusion

This study confirms, on the one hand, the results of previous studies (e.g. Schulze et al., 2022; Kersten and Lindstedt, 2022; Przybilla et al., 2020), which were mostly conducted in flat or moderate terrain in favorable conditions, and, on the other hand, provides important new insights: The acquisition of 3D point clouds of complex terrain with accuracies of a few centimetres is made possible through the use of advanced image processing strategies, direct measurement of image positions, and complex flight patterns such as cross-grid and oblique image flights. These strategies include self-calibration through standard and Fourier series modeling. It is noteworthy that this can be achieved without using GCPs, even if the RTK-GNSS positioning is subject to irregularities. Spatial deformations such as doming or bowling are not detectable. Variations in the GSD due to the flight altitude (above ellipsoid / above ground) do not appear to have a significant influence on the resulting accuracies, although the stability of the image block is improved with an almost constant GSD as well as the density of the resulting point clouds are more homogeneous.

This also demonstrates the potential of relatively inexpensive UAS such as the DJI Phantom 4 RTK for monitoring difficult-to-access study areas where the use of GCPs is impossible. Nevertheless, for reasons of independent quality control we do not advise against the use of GCPs and recommend integrating at least one GCP, e.g., the starting point of the UAS, into the evaluations. Furthermore, the use of CPs is recommended for an independent control of the results.

Acknowledgement

We kindly thank PhD Liss Marie Andreassen and the Jotunheimen National Park Management for supporting and authorising the UAS flights and Kartverket for providing the CPOS service.

References

Andreassen, L. M., Elvehøy, H., Kjøllmoen, B., Belart, J. M. C., 2020. Glacier change in Norway since the 1960s – an overview of mass balance, area, length and surface elevation changes. *Journal of Glaciology*, 66(256), 313–328.

Belloni, V., Fugazza, D., Di Rita, M., 2022. UAV-based Glacier Monitoring: GNSS Kinematic Track Post-Processing and Direct Georeferencing for Accurate Reconstructions in Challenging Environments. *Int. Arch. Photogramm. Remote Sens. Spatial Inf. Sci.*, XLIII-B1-2022, 367–373.

Brown, D., 1971. Close-Range Camera Calibration. *Photogrammetric Engineering*, 37, 855–866.

Eltner, A., Schneider, D., 2015. Analysis of Different Methods for 3D Reconstruction of Natural Surfaces from Parallel-Axes UAV Images. *The Photogrammetric Record*, 30(151), 279–299.

Eltner, A., Sofia, G., 2020. *Structure from motion photogrammetric technique*. Elsevier, chapter 1, 1–24.

Gerke, M., Przybilla, H.-J., 2016. Accuracy Analysis of Photogrammetric UAV Image Blocks: Influence of Onboard RTK-GNSS and Cross Flight Patterns. *Photogrammetrie - Fernerkundung - Geoinformation*, 2016(1), 17–30.

Girod, L., 2021. The P4 RTK and D-RTK2 are a joke (post no. 6). forum.dji.com/thread-248710-1-1.html (25 January 2024).

Hastedt, H., Luhmann, T., Przybilla, H.-J., Rofallski, R., 2021. Evalulation of Interior Orientation Modelling for Cameras with Aspheric Lenses and Image Pre-Processing with Special Emphasis to SFM Reconstruction. *Int. Arch. Photogramm. Remote Sens. Spatial Inf. Sci.*, XLIII-B2-2021, 17–24.

Isfort, S., Elias, M., Maas, H.-G., 2024. Development and Evaluation of a Two-Staged 3D Keypoint Based Workflow for the Co-Registration of Unstructured Multi-Temporal and Multi-Modal 3D Point Clouds. *ISPRS Ann. Photogramm. Remote Sens. Spatial Inf. Sci.* [accepted].

James, M. R., Antoniazza, G., Robson, S., Lane, S. N., 2020. Mitigating systematic error in topographic models for geomorphic change detection: accuracy, precision and considerations beyond off-nadir imagery. *Earth Surface Processes and Landforms*, 45(10), 2251–2271.

James, M. R., Robson, S., 2014. Mitigating systematic error in topographic models derived from UAV and ground-based image networks. *Earth Surface Processes and Landforms*, 39(10), 1413–1420.

Kersten, T. P., Lindstedt, M., 2022. UAV-basierte Bildflüge mit RTK-GNSS – brauchen wir da noch Passpunkte? *UAV 2022 – Innovation und Praxis. DVW-Schriftenreihe*, 100, DVW e. V., Augsburg, 39–58.

Lague, D., Brodu, N., Leroux, J., 2013. Accurate 3D comparison of complex topography with terrestrial laser scanner: Application to the Rangitikei canyon (N-Z). *ISPRS Journal of Photogrammetry and Remote Sensing*, 82, 10–26.

Liebold, F., Mader, D., Sardemann, H., Eltner, A., Maas, H.-G., 2023. A Bi-Radial Model for Lens Distortion Correction of Low-Cost UAV Cameras. *Remote Sensing*, 15(22).

Liu, X., Lian, X., Yang, W., Wang, F., Han, Y., Zhang, Y., 2022. Accuracy Assessment of a UAV Direct Georeferencing Method and Impact of the Configuration of Ground Control Points. *Drones*, 6(2), 30.

Nesbit, P., Hugenholtz, C., 2019. Enhancing UAV–SfM 3D Model Accuracy in High-Relief Landscapes by Incorporating Oblique Images. *Remote Sensing*, 11(3), 239.

Pfeffer, W. T., Arendt, A. A., Bliss, A., Bolch, T., Cogley, J. G., Gardner, A. S., Hagen, J.-O., Hock, R., Kaser, G., Kienholz, C., Miles, E. S., Moholdt, G., Mölg, N., Paul, F., Radić, V., Rastner, P., Raup, B. H., Rich, J., Sharp, M. J., 2014. The Randolph Glacier Inventory: a globally complete inventory of glaciers. *Journal of Glaciology*, 60(221), 537–552.

Przybilla, H.-J., Bäumker, M., Luhmann, T., Hastedt, H., Eilers, M., 2020. Interaction Between Direct Georeferencing, Control Point Configuration and Camera Self-Calibration for RTK-Based UAV Photogrammetry. *Int. Arch. Photogramm. Remote Sens. Spatial Inf. Sci.*, XLIII-B1-2020, 485–492.

Sanz-Ablanedo, E., Chandler, J. H., Ballesteros-Pérez, P., Rodríguez-Pérez, J. R., 2020. Reducing systematic dome errors in digital elevation models through better UAV flight design. *Earth Surface Processes and Landforms*, 45(9), 2134–2147.

Schulze, R. G., Mader, D., Eltner, A., 2022. Genauigkeitspotential direkt georeferenzierter UAS-Messungen am Beispiel eines Bahnhaltepunktes. *Beiträge der 42. Wissenschaftlich-Technischen Jahrestagung der DGPF in Dresden, Publikationen der DGPF e.V.*, 30, Kersten, T.P. Tilly, N., Hamburg, Köln, 243–255.

Stark, M., Heckmann, T., Piermattei, L., Dremel, F., Kaiser, A., Machowski, P., Haas, F., Becht, M., 2021. From consumer to enterprise grade: How the choice of four UAS impacts point cloud quality. *Earth Surface Processes and Landforms*, 46(10), 2019–2043.

Tang, R., Fritsch, D., Cramer, M., 2012. New rigorous and flexible Fourier self-calibration models for airborne camera calibration. *ISPRS Journal of Photogrammetry and Remote Sensing*, 71, 76-85.

Terratec, 2020. NDH Jostedalsbreen 2pkt 2020. hoydedata.no (25 January 2024).